P. Vujkovic-Cvijin, J. Lee, B. Gregor, N. Goldstein, and R. Panfili, and M. Fox, "Infrared Transform Spectral Imager," Proc. SPIE 8520, Unconventional Imaging and Wavefront Sensing 2012, 85200K, (2012).

See next page.

Infrared transform spectral imager

Pajo Vujkovic-Cvijin[*], Jamine Lee, Brian Gregor, Neil Goldstein, Raphael Panfili and Marsha Fox

Spectral Sciences, Inc., 4 Fourth Avenue, Burlington, MA 01803-3304

ABSTRACT

A dispersive transform spectral imager named FAROS (FAst Reconfigurable Optical Sensor) has been developed for high frame rate, moderate-to-high resolution hyperspectral imaging. A programmable digital micromirror array (DMA) modulator makes it possible to adjust spectral, temporal and spatial resolution in real time to achieve optimum tradeoff for dynamic monitoring requirements. The system's F/2.8 collection optics produces diffraction-limited images in the mid-wave infrared (MWIR) spectral region. The optical system is based on a proprietary dual-pass Offner configuration with a single spherical mirror and a confocal spherical diffraction grating. FAROS fulfills two functions simultaneously: one output produces two-dimensional polychromatic imagery at the full focal plane array (FPA) frame rate for fast object acquisition and tracking, while the other output operates in parallel and produces variable-resolution spectral images via Hadamard transform encoding to assist in object discrimination and classification. The current version of the FAROS spectral imager is a multispectral technology demonstrator that operates in the MWIR with a 320 x 256 pixel InSb FPA running at 478 frames per second resulting in time resolution of several tens of milliseconds per hypercube. The instrument has been tested by monitoring small-scale rocket engine firings in outdoor environments. The instrument has no macro-scale moving parts, and conforms to a robust, small-volume and lightweight package, suitable for integration with small surveillance vehicles. The technology is also applicable to multispectral/hyperspectral imaging applications in diverse areas such as atmospheric contamination monitoring, agriculture, process control, and biomedical imaging, and can be adapted for use in any spectral domain from the ultraviolet (UV) to the LWIR region.

Keywords: spectral imaging, multispectral, hyperspectral, infrared, digital micromirror array, Hadamard transform, standoff sensing, tracking

1. INTRODUCTION

Spectral imaging sensors use emitted or reflected light emanating from a distant scene to detect and characterize the objects within the scene. The light reaching the sensor is spectrally dispersed and intensities of discrete spectral bands are measured. The resulting spectra contain information on unique spectral signatures of the object and can be used to identify the object and/or measure its relevant features. Spectral imagers assign spectra to each pixel of the recorded two-dimensional spatial image and generate a dataset known as hypercube. Optical sensors based on various modalities of spectral imaging are rapidly coming into use in many commercial (process control, agriculture and food industry, biomedical instrumentation, forensics) and government (surveillance sensors, chemical/ biological/pollution sensing, explosive detection) applications.

Fast spectral imaging sensors are needed for monitoring highly energetic events where identifying the composition of released material following the event is of interest. A dispersive transform spectral imager named FAROS (FAst Reconfigurable Optical Sensor) has been developed at Spectral Sciences Inc. for high-frame rate, moderate-to-high-resolution spectral imaging applications. It simultaneously produces both instantaneous spatial polychromatic imagery for object acquisition and tracking and spectrally resolved images in the mid-wave infrared (MWIR) spectral region for object discrimination and classification.   The spatial, spectral and temporal resolution of the data produced by FAROS are adjustable in real time, making it possible to achieve optimum tradeoff between different sensing functions in order to meet the dynamic monitoring requirements typically encountered in relevant applications. The instrument is of compact size and contains no macro-scale moving parts, which makes it suitable for airborne and spaceborne applications.

In this paper, we describe the instrument concept and the design of the FAROS sensor and present the results of FAROS prototype testing carried out by monitoring small-scale rocket engine firings in an outdoor environment.

*pajo@spectral.com; phone 1 781 273-4770; fax 1 781 270-1161; www.spectral.com

2. INSTRUMENT CONCEPT

The principles of operation of a dispersive transform imaging spectrometer are illustrated on Figure 1[1-3]. The instrument uses two polychromators with a two-dimensional spatial light modulator (SLM) placed in the intermediate image plane between them. The first polychromator disperses the image into spectral components and images them onto the SLM. The SLM spectrally encodes the image by modulating the intensity of selected spectral bands in the dispersed image. The encoded image is then spectrally recombined by the second polychromator and imaged onto a focal plane array (FPA) (Figure 1).

Spectral encoding is performed by SLM whose array elements are individually addressable and small relative to the spatial/spectral resolution elements. The SLM can be programmed to generate a dynamic series of spatial patterns (masks) that implement the transform function. Possible transform functions include traditional single-slit wavelength scanning, multiple-slit filtering, Hadamard transform[4] multiplexed spectroscopy, and the "matched filter" transform, where the SLM is used to produce a spectral mask that brings out known distinctive spectral features of the target relative to those of the background[3].
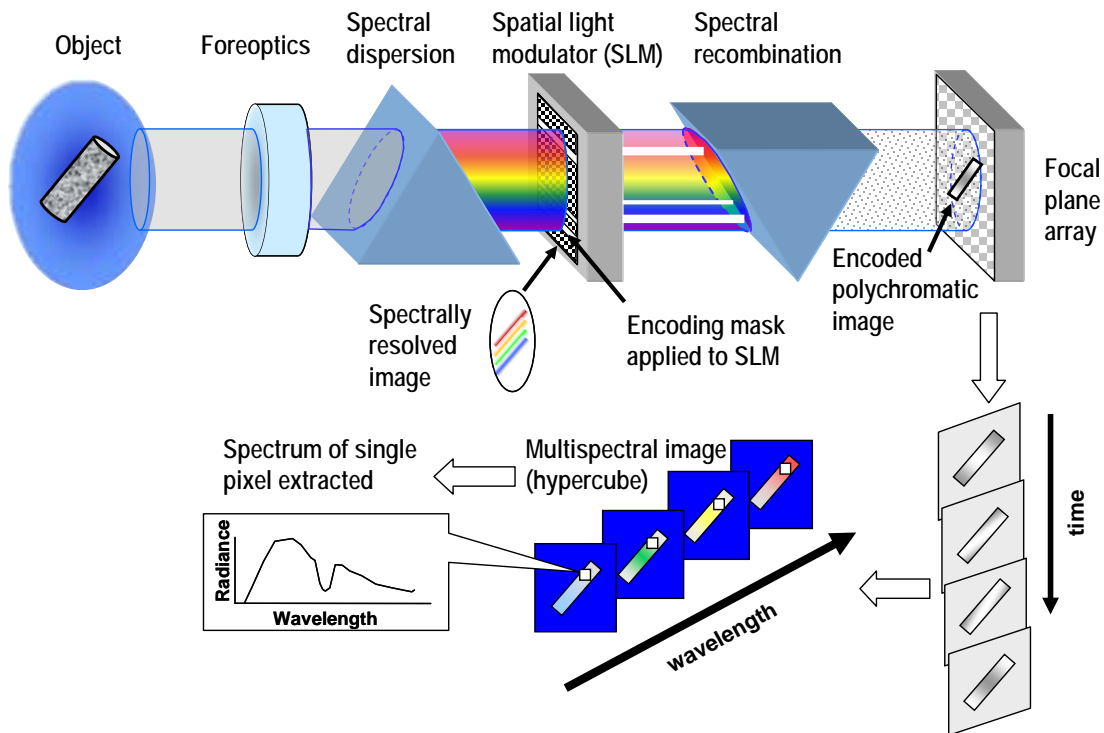

Figure 1. Dispersive transform imaging spectrometer principle of operation: light from the object is dispersed, dynamically encoded with a series of masks, and recombined on the detector.

The FAROS spectral imager uses a reflective Digital Micromirror Array (DMA)[5] as the SLM to perform binary on-off modulation to spectrally encode two-dimensional images, resulting in the generation of multispectral or hyperspectral images ("hypercube"). Hadamard transform was chosen as the transform function for FAROS because of its multiplexing capability and its processing speed. To implement Hadamard transform, the DMA is programmed with a series of binary masks based on Simplex (S) matrices, where elements 0 and 1 translate into on-off modulation of individual micromirror pixels of the DMA. Recording a N-band spectrum in this way requires N masks based on a set of N matrices resulting in $(N-1)^{1/2}/2$ multiplex (Felgett's) advantage in the signal to noise ratio (SNR) relative to the single-slit scanning approach. The multiplexing feature of the Hadamard transform makes it possible to collect the light contained in approximately half of all spectral bands simultaneously, thereby providing the much needed photon collection efficiency in the typically photon-starved IR spectral region where FAROS operates. The images recorded by the FPA are decoded by the inverse Hadamard transform which retrieves the spectrum of each pixel in order to construct the hypercube (Figure 1).

Due to its unique design based on the disperse-encode-recombine approach, the FAROS spectral imager provides two outputs simultaneously: one output produces polychromatic spatial images at the maximum frame rate of the FPA, while the other output produces spectral images at a sub-multiple frame rate. The polychromatic output can be used for fast object acquisition and tracking, while spectral images can be used for object discrimination and classification with lower temporal resolution. By selecting the appropriate transform function, together with the desired spatial/spectral/temporal data acquisition parameters, and applying such function to the SLM, the type of information collected and its structure can be adjusted in real time.

3. INSTRUMENT DESIGN

Figure 2 shows a schematic representation of the FAROS optical system. The system can use any standard infrared objective as its foreoptics. It is currently configured with a 3 inch diameter, 100mm focal length, F/2.3 ZnSe multielement objective manufactured by Stingray Optics, designed for diffraction limited performance in both LWIR and MWIR spectral range. The foreoptics creates an image at the entrance plane of the core spectrometer. The spectrometer uses a dual-pass design with a single concave mirror and a single convex grating to disperse, encode and recombine the light[6]. The design is based on the Offner relay, with two nearly concentric spherical surfaces of which the inner convex surface is diffractive. The light makes two passes through the system, one to disperse the image and one to recombine the image, with spectral encoding applied by the DMA to the dispersed image in the intermediate plane between the two passes (Figure 2.). The dispersed image is produced with 1:1 magnification. A pickoff mirror directs the output image to the FPA. The concave primary mirror is a 180mm diameter gold-coated Zerodur spherical concave mirror with a radius of curvature of 200mm. The gold-coated convex grating is rectangular 34x80mm, with the radius of curvature of 100 mm. The grating is machined by diamond turning with a groove density of 13 lines/mm and a blaze angle of 3.5degrees. The system is designed to cover the spectral range 7-13µm (LWIR) in the first order or 3.5-6.5µm (MWIR) in the second order of the grating. The object field has the dimension of 5 x 8mm. The system has an effective F number of F/2.8. It provides near-diffraction-limited image quality at the output image plane in both diffraction orders. Three factors contribute to high imaging quality of this design: 1) the dispersion plane and offset plane are perpendicular to each other, 2) the object and dispersed image points are very close to the optical axis, and 3) the grating center of curvature is slightly displaced relative to the outer mirror center of curvature in order to control the third order astigmatism and coma.

The transform-encoding spatial light modulator used in our system is a DMA consisting of 1024x768 aluminum-coated silicon micromirrors measuring 13.8µm x 13.8µm each (14.1mm x10.6 mm total aperture). The DMA chip is a commercial Texas Instruments DMD 0.7 XGA 12° DDR chip modified by replacing the original window with a custom AR-coated ZnSe window for IR operation. The DMD 0.7 XGA 12° DDR chip is used here with a Discovery 1100 control board and an Accessory Light modulator Package (ALP) for high-speed operation, both supplied by Texas Instruments/Digital Light Innovation.

In the experiments described in this paper, the system operates in the MWIR spectral range in the second order of the grating. The output image is recorded by a Santa Barbara Focal Plane/Lockheed Martin SBF-200 camera with a 320x256 pixel liquid-nitrogen cooled InSb FPA operating in the MWIR spectral range (~1.5-5.3µm). The camera communicates with the host computer through a CameraLink interface and a National Instruments PCIe 1427 frame grabber. The maximum camera frame rate for the full 320x256 pixel resolution is 478 Hz, provided by FPA's fast digital readout circuitry. The camera operation is synchronized with that of the DMA by the computer program that runs the instrument. The output image plane of the optical system is tilted relative to the optical axis by 12°, as a consequence of the angle at which the DMA reflects the image to perform on-off switching. In order to position the FPA at an angle relative to the optical axis, the internal cold stop and the front window mount of the SBF-200 camera had to be modified.
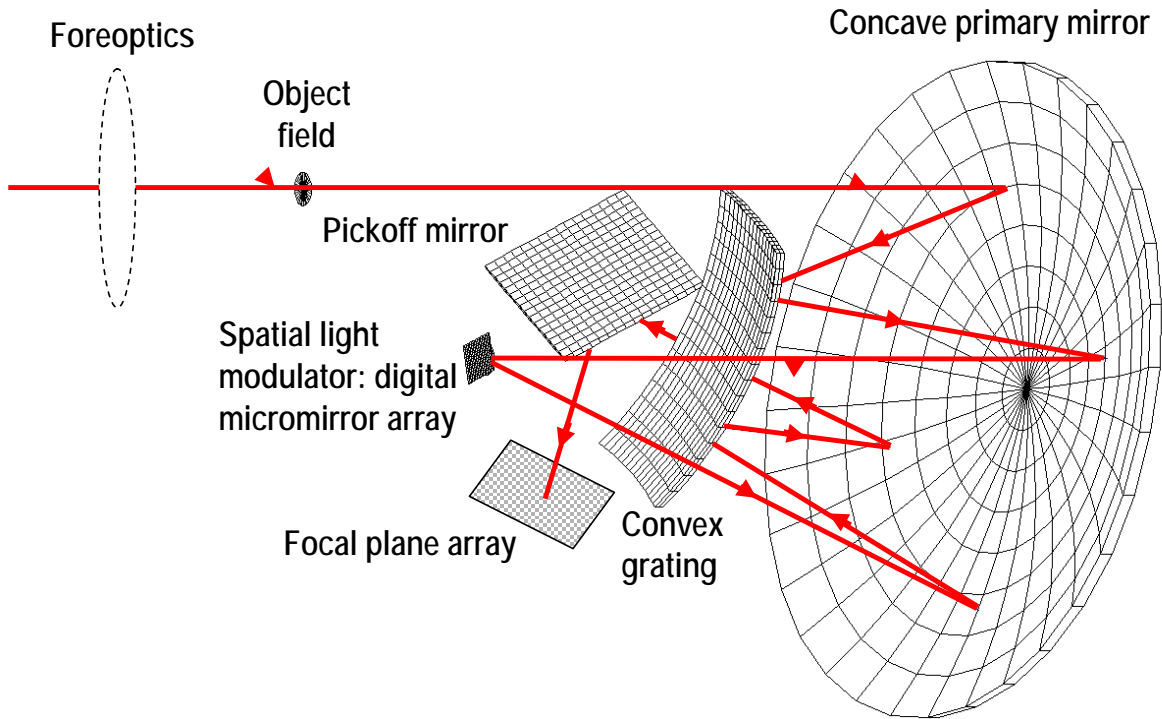
Figure 2. FAROS optical system design.

While the DMA-based spectral imager design of Figure2 has been demonstrated to be effective, the use of currently commercially available DMAs designed for the visible spectral range is challenging in the M/LWIR. Micromirrors of dimensions 13.8μm x 13.8μm are comparable in size to the wavelength of light in the M/LWIR, making diffraction effects on these apertures significant. The DMA acts as a grating, deflecting the incoming radiation at a wavelength-dependent angle. However, the collection angle afforded by our F/2.8 system is large enough to collect the majority of the deflected radiation with a wavelength dependent variation in the recombined focal plane not larger than several percent of the maximum intensity.

In a separate set of experiments we measured the modulation efficiency of the Texas Instruments DMD 0.7 XGA 12° DDR chip and demonstrated collection efficiency of diffracted light as high as 80% in the MWIR (3-5μm) and 10-25% in the LWIR (7-13 μm)[3]. Such modulation efficiency is a limiting factor for DMA-based dispersive transform spectral imagers in the LWIR, indicating the need for the development of DMAs with substantially larger micromirrors consistent with long IR wavelengths[7].

4. EXPERIMENTAL RESULTS

The FAROS spectral imager was tested in the field by monitoring the firings of model rocket engines. Model rocket engines are convenient test objects to simulate energetic events due to their compactness and safety while producing a plume showing both spatial variation and spectral agility. We measured the plume signature of the ESTES B6-4 model rocket engine[8] whose propellant is a mixture of potassium nitrate, sulfur and charcoal/sugar. The rocket engine was clamped down on a stand located 10 meters away from the FAROS sensor. The rocket plume lasted approximately 4 seconds.

We operated the SBF-200 camera at its highest frame rate, 478 Hz, and set the camera exposure to 2.11 ms, near its full duty cycle. For calibration purposes, a pair of DMA frames with all micromirrors turned on and all micromirrors turned off was added at the beginning of each set of DMA Hadamard transform masks. Hadamard masks with either 23 or 83 spectral channels were used. Each set of Hadamard masks produced a 320×256 pixels × (23 channels or ×83 channels) hypercube that captured spatial and spectral signature of the target. Only a portion of the 23 or 83 channel set collected

spectral information contained in the second order of the grating (3.5-6.5µm). A background image file was taken prior to the ignition of the rocket motor with the instrument input aperture covered with absorbing material at the ambient temperature in order to remove the instrument background contribution. Due to the memory size and CPU speed limitation of our PC computer, the camera operation needed to be interrupted for data processing and storage resulting in 12 sets continuously collected without interruption for the 23 channel operation, and 1 set collected for the 83 channel operation.

For the 23-channel data, spectral images of the plume transient event were captured with 12 sets of 25 (23 bands +2 on/off) frames with the time resolution of 52ms over the total acquisition period of 628ms. Out of 23 recorded spectral channels, 7 channels covered the spectral region 3.5 µm -5.1µm in the second order of the grating. Figure 3 shows the spatial/spectral/temporal data taken during the first 628ms of rocket engine firing. Figure 3 (a) shows the spatial image of the plume, obtained by taking the difference between on- and off-frames and averaging over 12 collected sets. The cursor shows the location of the pixel (112, 131) whose spectral and temporal information is displayed on Figures 3 (b), (c) and (d). Figure 3(b) shows the time-dependent spectral transient of this pixel represented by seven spectral bands covering the 3.5µm – 5.1µm region taken in 52ms intervals. Each spectrum on Figure 3(b) is represented by a horizontal row, with color-coded intensity, and with consecutive spectra progressing in time along the vertical direction. Figure 3(c) shows the averaged spectrum at pixel (112, 131) as collected over the acquisition interval, where the peak at 4.31µm corresponds to the emission from hot CO_2 gas contained in the plume. Hot CO_2 is the most prominent product of combustion detectable in this spectral range. Strong emission from hot CO_2 at 4.31µm also dominates the time-resolved spectra shown on Figure 3(b). Figure 3(d) shows the time history of the emission intensity of the hot CO_2 peak at pixel (112, 131) over the entire acquisition period, revealing intensity fluctuations of approximately ± 12% around the average radiance.

(a)   (b)
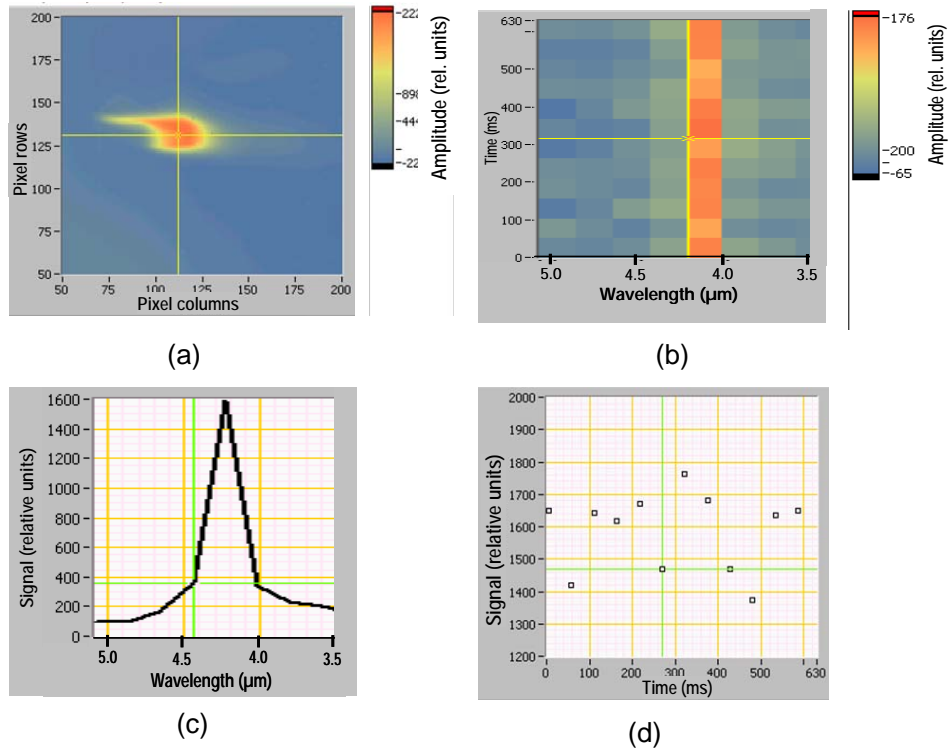

(c)   (d)

Figure 3. Spatial/spectral/temporal data at the beginning of the rocket engine firing: (a) panchromatic spatial image of the plume; (b) time dependent spectral transient of the selected pixel; (c) spectrum of the selected pixel over the acquisition interval showing the 4.31µm hot CO_2 emission peak; (d) time history of the 4.31µm CO_2 emission peak (relative units) at the selected pixel over the acquisition period.

Figure 4 shows the spatial/spectral/temporal data collected close to the end of the rocket engine firing. In this case, data acquisition started ~3 seconds after the engine was fired. The spatial image at Fig 4(a) shows that the location of the main plume emission has changed, and that the emission at the previous location (112, 131) decreased substantially. Figure 4(b) shows the spectral transient for this cycle, with data arranged the same way as on Figure 3(b). The plume activity was characterized again by hot CO_2 emission at 4.31µm, as in the previous cycle. Figure 4(c) shows the spectrum at pixel (112, 131) collected over the acquisition period, where the hot CO_2 emission decreased by a factor of 7 relative to the intensity at the beginning of firing. Figure 4(d) shows the dynamics of the plume in this time interval where the hot CO_2 emission decayed rapidly from 75% of the intensity at the beginning of firing, to close to zero after approximately 150ms.
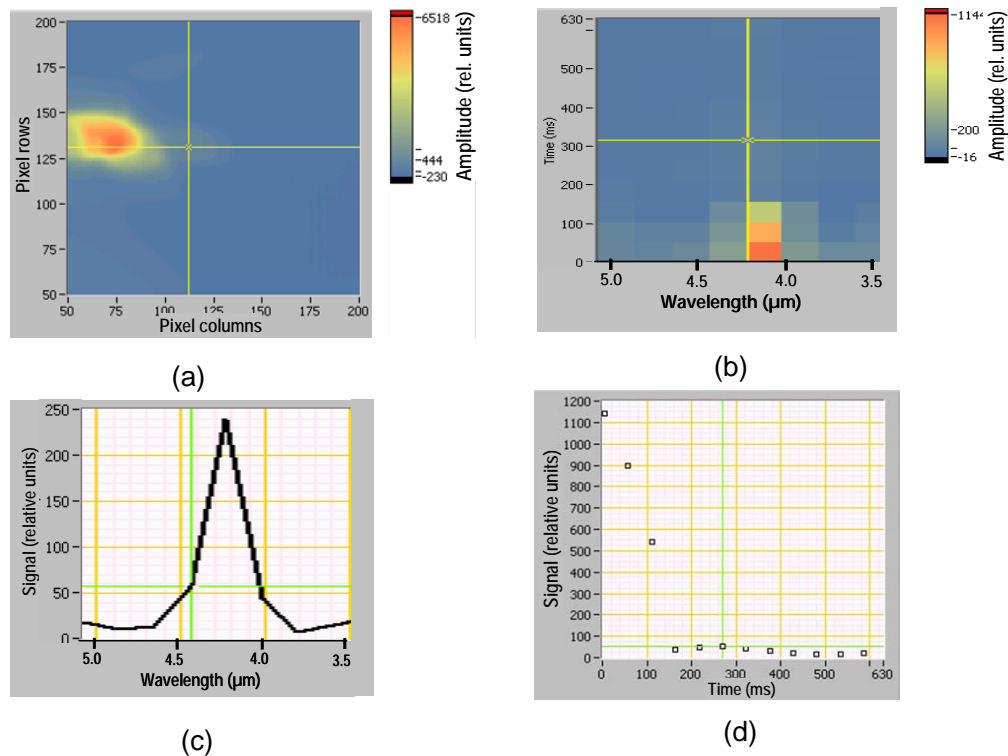

(a)

(b)

(c)

(d)

Figure 4. Spatial/spectral/temporal data close to the end of rocket engine firing: (a) panchromatic spatial image of the plume; (b) time dependent spectral transient of the selected pixel; (c) spectrum at the selected pixel showing the 4.31µm hot CO_2 emission peak; (d) time history of the 4.31µm hot CO_2 emission intensity (relative units) at the selected pixel over the acquisition period.

The results of the FAROS sensor operating with 83 spectral channels are presented on Figure 5. In this case, one spectral scan was completed in 180ms. Out of 83 recorded spectral channels, 23 channels covered the spectral region 3.5 µm -5µm in the second order of the grating. Figure 5 shows spatial/spectral data taken 1.1 seconds after the engine was fired. Figure 5(a) shows the spatial intensity distribution while Figure 5(b) shows spectral data for pixel (172, 125) collected over one 180ms cycle of spectral data acquisition. The spectrum presented on Figure 5 shows the target spectrum in higher resolution relative to the 7-band spectra on Figs. 3 and 4 and therefore it reveals a "biteout" on the blue-side wing of the hot CO_2 emission peak. This biteout is due to the atmospheric CO_2 absorption centered at 4.27µm, as described in detail in the next section.
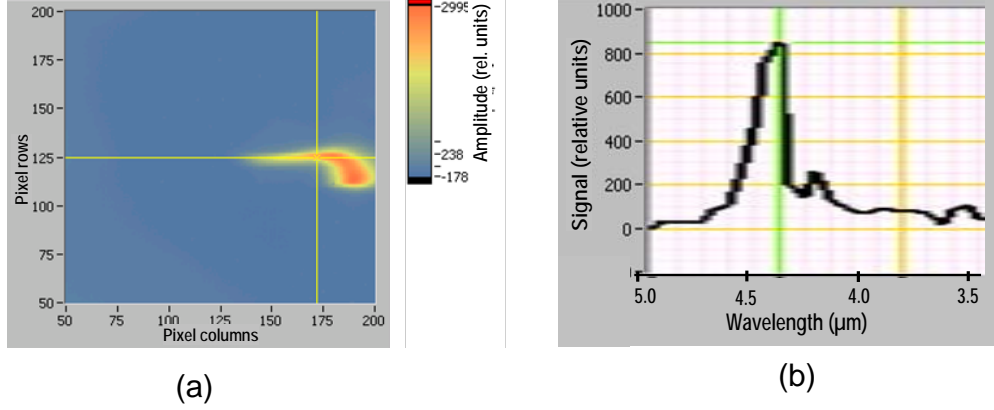
(a)

(b)

Figure 5. Spatial/spectral data taken at 23-band spectral resolution: (a) spatial image of the plume; (b) spectrum at the selected pixel.

5. DATA ANALYSIS

The spectral signature recorded by the FAROS spectral imager shown on Figure 5 (b) can be described as path radiance I_ν arising from emission and absorption defined by the radiation transport equation (1) which includes local radiance source S_ν at frequency ν, observed by a sensor at a distance s

$$I_\nu = S_\nu \cdot t_\nu + \int_0^s t_\nu(r) \cdot \sum_\ell J_{\nu,\ell}(r) \cdot \kappa_{\nu,\ell}(r) \cdot \rho_\ell''(r) \cdot dr \tag{1}$$
,

where t is the transmission, J is a source term, κ is an absorption coefficient, and ρ'' is the column density of the lower state of a transition for the molecular species ℓ. If we assume uniform layers, the integral in the above expression can be replaced by a summation over layers.

We model the emissions observed from a hot plume by assuming three layers. The first and last layers are assumed to conform to ambient temperatures, pressures, and concentrations, while the middle layer represents the plume at elevated temperature with high CO_2 concentration. Path radiance at a specific frequency ν can then be expressed as:

$$I_\nu = B_\nu\left(T^{(m)}\right) \cdot \left(1 - t_\nu^{(m)}\right) \cdot \sum_{m'=1}^{m-1} t_\nu^{(m')} \tag{2}$$
,

where the superscripts refer to the layer index (m), the source term is replaced by the Planck function (B), and T refers to the local temperature. The layer transmission contains all the line information

$$t_\nu(T) = \exp(-\tau_\nu(T)) = \exp\left(-\sum_\ell \tau_{\nu,\ell}(T)\right) = \exp\left(-\sum_\ell \kappa_{\nu,\ell}(T) \cdot \rho_\ell''(T) \cdot s\right) \tag{3}$$
,

while the absorption coefficient is a function of the line center strength S and line shape profile f:

$$\kappa_{\nu,\ell}(T) = S_\ell(T) \cdot f_{\nu,\ell}(T) \tag{4}$$
.

A proper treatment of the line shape profile will simultaneously take into account both temperature and pressure broadening under the assumption that the two quantities are independent variables. The combined line shape is modeled as a Voigt profile, a convolution of the Doppler-broadened f_D and pressure-broadened f_L line shapes[9]:

$$f_V(\nu, \nu_0) = \int f_L(\nu' - \nu_0) \cdot f_D(\nu - \nu') \cdot d\nu' \qquad (5)$$

In this analysis we utilize the SAMM code, a well-established tool to compute observed radiance based on the line-by-line radiation transport model[10]. SAMM is a flexible tool for computing atmospheric background radiance and transmission in the 0.3 to 40 µm (250 to 33,000 cm^{-1}) wavelength region, for arbitrary line-of-sight from 0 to 300 kilometers in altitude. While spectroscopic information within SAMM is usually obtained from the HITRAN database[11], in this analysis we have used the HITEMP database[12], a high-temperature extension to HITRAN. This substitute is necessary given the elevated temperatures we encounter in this analysis. Atmospheric information is provided to SAMM via an external file. We use conditions consistent with the ground layer of the U.S. 1976 standard atmosphere[13] for our ambient conditions. For our plume conditions, we construct an atmosphere whose total pressure (P) matches the ground pressure of the ambient atmosphere. This amounts to ensuring the product of the total molecular density (ρ) and temperature remains a constant:

$$P \propto \rho \cdot T \qquad (6)$$

Besides gaseous components, the plume of the model rocket engine contains a certain amount of soot which we modeled using curves generated by the theory of Lee and Tien[14], resulting in spectral dependency that is remarkably linear in our spectral region. We assumed that soot is composed entirely of carbon and that it is emitting broadband radiation at the same temperature as the flame. The contribution of the soot radiance around the 4.3µm band was found to be between 1% and 2% of the total radiance in our case.

A radiation transport algorithm developed specifically for monitoring hot gas exhaust in the ambient environment has been developed recently at Spectral Sciences Inc. based on our existing SAMM code[15-17]. The approach incorporates computational fluid dynamic (CFD) simulation of the combustion process as a local atmospheric region in SAMM. Observed radiance from lines-of-sight intersecting both the ambient environment and the CFD region as well as radiance originating from molecules not present in the ambient environment can be computed by our new hot gas exhaust code[17].

The model rocket engine plume whose signature is shown on Figure 5 is modeled here with three layers and is therefore considerably more straight-forward than the general case. The path radiance shown in Equation 2 can be explicitly written as:

$$I_\nu = B_\nu\left(T^{(1)}\right) \cdot \left(1 - t_\nu^{(1)}\right) + B_\nu\left(T^{(2)}\right) \cdot \left(1 - t_\nu^{(2)}\right) \cdot t_\nu^{(1)} + B_\nu\left(T^{(3)}\right) \cdot \left(1 - t_\nu^{(3)}\right) \cdot t_\nu^{(2)} \cdot t_\nu^{(3)} \qquad (7)$$

where the superscript in parentheses refers to the index of the layer. For our case, the first and last layers are both modeled as 10 meter segments and assumed to be at ambient temperatures and atmospheric concentrations. The middle layer is modeled as a 10 centimeter segment with ambient pressure. The central layer (2) is more complicated in that molecules and soot will radiate at different temperatures. We can re-express an effective black body function as a simple combination of these two elements, labeled "molecular" for molecular temperature and transmission and "soot" for soot temperature and transmission.

$$B_\nu\left(T^{(2)}\right) = \frac{B_\nu\left(T_{molecular}^{(2)}\right) \cdot \ln\left(t_{\nu,molecular}^{(2)}\right) + B_\nu\left(T_{soot}^{(2)}\right) \cdot \ln\left(t_{\nu,soot}^{(2)}\right)}{\ln\left(t_{\nu,molecular}^{(2)}\right) + \ln\left(t_{\nu,soot}^{(2)}\right)} \qquad (8)$$

where the broadband absorption coefficients of soot guarantee the denominator is never zero.

The result of modeling is presented in Figure 6, along with measured data deconvolved for the instrument response function. The high resolution output of the line-by-line spectral modeling algorithm was convolved with a triangular slit function whose full-width at half-maximum was 40 cm^{-1}, corresponding to the instrument's spectral resolution in this case. Soot is modeled as emitting at the same temperature as the flame, while the plume molecular emission is radiating at a lower temperature (Figure 5(a)). A value of 22% CO_2 concentration, where nearly all of the available

oxygen is utilized in combustion, and the plume temperature of 1200 K give a good agreement with the measured data presented in Figure 6. Such agreement between the measured and modeled data illustrates the spectral fidelity of the FAROS spectral imager.
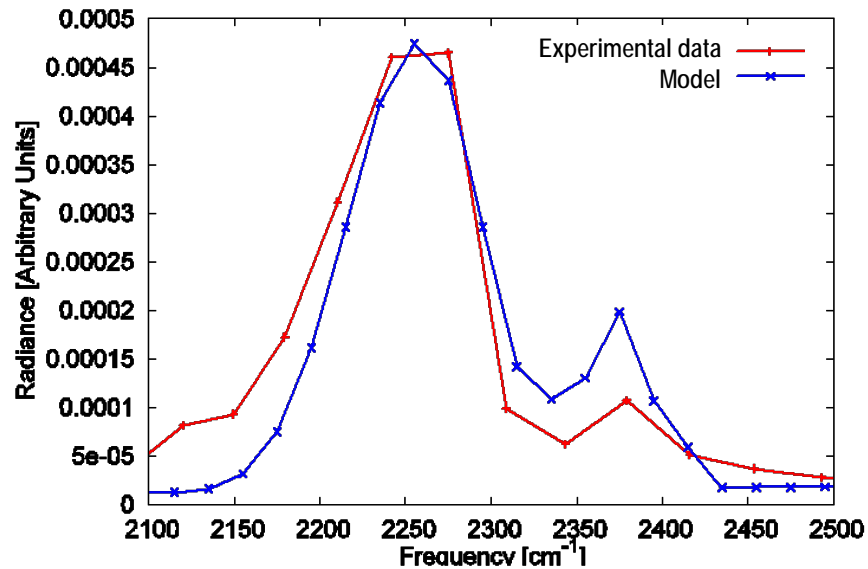

Figure 6. Comparison of the experimental and modeled data for the hot CO_2 emission feature shown on Figure 5.

6. CONCLUSIONS

The FAROS dispersive transform spectral imager has been developed for high-frame rate spectral imaging in the MWIR spectral region. A programmable digital micromirror array (DMA) modulator makes it possible to adjust spectral, spatial and temporal resolution in real time to achieve optimum sensing parameter tradeoff for dynamic monitoring requirements. The instrument has been tested by monitoring model rocket engine firings in an outdoor environment. The instrument has no macro-scale moving parts, and conforms to a robust, small-volume and lightweight package, suitable for integration with small surveillance vehicles or with industrial sensor suites. The architecture of the FAROS sensor can be replicated in other spectral regions from the ultraviolet (UV) to the LWIR to address applications as diverse as chemical/biological sensing, chemical and biomedical imaging, process control and various modalities of standoff monitoring.

ACKNOWLEDGMENT

REFERENCES

[1] Vujkovic-Cvijin, P., Goldstein, N., Fox, M.J., Higbee, S.D., Latika S. Becker L.C., and Teng K. Ooi, T.K. "Adaptive Spectral Imager for Space-Based Sensing", Proc. SPIE Vol. 6206, paper 6206-33 (2006).
[2] Goldstein N., Pajo Vujkovic-Cvijin; Marsha Fox; Steven Adler-Golden; Jason Cline; Brian Gregor; Jamine Lee; Alan C. Samuels; Shawn D. Higbee; Latika S. Becker; Teng Ooi, "Programmable Adaptive Spectral Imagers for Mission-Specific Application in Chemical/Biological Sensing", International Journal of High Speed Electronics and Systems (IJHSES), Vol. 17, 749 - 760 (2007).

[3] Goldstein, N., P. Vujkovic-Cvijin, M. Fox, B. Gregor, J. Lee, J. Cline, and S. Adler-Golden "DMD-based adaptive spectral imagers for hyperspectral imagery and direct detection of spectral signatures," SPIE Vol. 7210,721008-1-721008-8 (2009).

[4] Harwit, M. and N.J.A. Sloane, "Hadamard Transform Optics", Academic Press, NY, (1979).

[5] Hornbeck, L., "Deformable Mirror Spatial Light Modulator," Proc. SPIE, Vol. 1150, 86 (1989).

[6] Goldstein, N., P. Vujkovic-Cvijin, M. J. Fox, S. Adler-Golden, J. Lee, J.A. Cline, B. Gregor, "Spectral Encoder," US Patent 7,324,196 (2008).

[7] Reimer K., Engelke R., Witt M., Wagner B., "16 k Infrared Micromirror Arrays with Large Beam Deflection and Tenth Millimeter Pixel Size", Part of the SPIE Conference on Miniaturized Systems with Micro-Optics and MEMS, SPIE vol. 3878, pp. 272-280, (1999)

[8] Estes rockets, http://www.estesrockets.com/ (2012).

[9] Galatry, L., "Simultaneous Effect of Doppler and Foreign Gas Broadening on Spectral Lines," Phys. Rev., vol. 122, pp. 1218-1223 (1961).

[10] Dothe, H., Duff, J.W., Panfili, R., Gruninger, J.H., Kennett, R.G., Acharya, P.K., Berk, A., and Bernstein, L.S., "Users' Manual for SAMM® Version 3," Technical Report SSI-TR-599, (2010).

[11] Rothman, L.S., I.E. Gordon, A. Barbe, D. Chris Benner, P.F. Bernath, M. Birk, V. Boudon, L.R. Brown, A. Campargue, J.-P. Champion, K. Chance, L.H. Coudert, V. Dana, V. M.Devi, S. Fally, J.-M. Flaud, R.R. Gamache, A. Goldman, D. Jacquemart, I. Kleiner, N. Lacome, W.J. Lafferty, J.-Y. Mandin, S.T. Massie, S.N. Mikhailenko, C.E. Miller, N. Moazzen-Ahmadi, O.V. Naumenko, A.V. Nikitin, J. Orphal, V.I. Perevalov, A. Perrin, A. Predoi-Cross, C.P. Rinsland, M. Rotger, M. Simeckova, M.A.H. Smith, K. Sung, S.A. Tashkun, J. Tennyson, R.A. Toth, A.C. Vandaele, and J. VanderAuwera, "The HITRAN 2008 Molecular Spectroscopic Database," J. Quant. Spectrosc. Radiat. Transfer 110, 533-572 (2009).

[12] Rothman, L.S., I.E. Gordon, R. J. Barber, H. Dothe, R.R. Gamache, A. Goldman, V.I. Perevalov, S. A. Tashkun, and J. Tennyson, "HITEMP, the high-temperature molecular spectroscopic database," J. Quant. Spectrosc. Radiat. Transfer 111, 2139-2150 (2010).

[13] Whitten, RC and Vaughan, WW, "Guide to Reference and Standard Atmosphere Models," AIAA, G-003C-2010, (2010).

[14] Lee, S.C. and Tien, C.L. "Effect of soot shape on soot radiation" Journal of Quantitative Spectroscopy and Radiative Transfer, 29, 259-265 (1983)

[15] Panfili, R., Vujkovic-Cvijin, P., Tan, X., Kennett, R, Taylor, R., Dothe, H., Bernstein, L., Smith, P.J., Thornock, J.N., Gross, K., and Seebold, J., "Remote Detection of Volatile Organic Compound Emissions from Combustion Flares," 33rd Annual Review of Atmospheric Transmission Models Meeting (2011)

[16] Panfili, R., H. Dothe, P. Vujkovic-Cvijin, X. Tan, R. Kennett, R. Taylor, L.S. Bernstein, P.J. Smith, J.N. Thornock, K. Gross, and J. Seebold, "High-fidelity modeling of flare combustion and emission detection," American Flame Research Committee Industrial Flares Colloquium (2011)

[17] Taylor, R. and R. Panfili, "Utilizing hyperspectral imagery to indentify highly-reactive volatile organic compounds in combustion flare emissions," IEEE Workshop on Hyperspectral Image and Signal Processing: Evolution in Remote Sensing (2012)